Exponential Time-Marching method for the Unsteady Navier-Stokes Equations

Conference Paper · January 2019

DOI: 10.2514/6.2019-0907

2 authors:

Shu-Jie Li
Beijing Computational Science Research Center
16 PUBLICATIONS **64** CITATIONS

SEE PROFILE

Lili Ju
University of South Carolina
105 PUBLICATIONS **1,944** CITATIONS

SEE PROFILE

AIAA SciTech Forum
7-11 January 2019, San Diego, California
AIAA Scitech 2019 Forum

10.2514/6.2019-0907

Exponential time-marching method for the unsteady Navier-Stokes equations

Shu-Jie Li*
Beijing Computational Science Research Center, Beijing, 100193, China
Lili Ju†
Department of Mathematics, University of South Carolina, Columbia, SC 29208, USA

In this paper, the predictor-corrector exponential (PCEXP) time marching scheme, originally developed by S.-J. Li, et al in AIAA-2017-0753 is extended to compute the time-dependent solutions of the compressible Navier-Stokes equations with high-order discontinuous Galerkin discretizations in space. The ability of PCEXP scheme that can greatly relax the restriction of time step due to the Courant-Friedrichs-Lewy (CFL) condition is investigated for the computations of unsteady laminar and turbulent flows with large time steps. It is observed that the PCEXP scheme yields accurately resolved solutions in regions of boundary layers and turbulent wakes. Numerical results demonstrate the applicability of PCEXP scheme to unsteady viscous flows in two and three dimensions.

I. Introduction

The unsteady Navier-Stokes equations are relatively difficult to be accurately while efficiently solved due to the challenges from the numerics and physics, such as multi-scale effects, high-aspect-ratio meshing, and numerical errors, corresponding respectively to the physical stiffness, geometric stiffness, and numerical stiffness. The geometric stiffness directly imposes a severe Courant-Friedrichs-Lewy (CFL) restriction which results in tiny time steps for explicit time-marching methods, as in the cases of direct numerical simulations (DNS) and large eddy simulations (LES) of turbulent flows, in which spatial discretizations of the computational domains are often associated with stretched or refined grids for capturing boundary layers and wake flows. To prevent numerical dissipation from damping unsteady flow structures of laminar and turbulent flows, high-order spatial discretizations are pursued in spite of their relatively higher cost compared to second-order methods. However, the overall computational performance of using high-order methods is even more time-consuming for the time-stepping stage. Consequently, efficient time-marching schemes are always required.

In our previous works, we have shown that the predictor-corrector exponential (PCEXP) scheme can relax the CFL restriction while maintaining low absolutely temporal errors.[1] In this paper, the advantages of PCEXP scheme for inviscid flows[1,2] and steady flows[3,4] are verified for unsteady viscous flow regime, by solving the time-accurate solutions of unsteady compressible Navier-Stokes equations. This paper is organized as follows. Section II outline the algorithm and implementation of the PCEXP scheme. Section III reports numerical results to demonstrate the accuracy of solving 2-D and 3-D laminar and turbulence flows. Finally, Secition IV concludes this work.

*Research Assistant Professor, Mechanics Division, No.10 West Dongbeiwang Road, Haidian District, Beijing 100193, China, E-mail: shujie@csrc.ac.cn. AIAA Member.
†Professor, Department of Mathematics, 1523 Greene Street Columbia, SC 29208, USA, E-mail: ju@math.sc.edu.

II. Predictor-Corrector EXPonential time integrator scheme (PCEXP)

Consider a semi-discrete ordinary differential equation (ODE) system obtained from a spatial discretization such as discontinuous Galerkin methods of the form

$$\frac{d\boldsymbol{u}}{dt} = \boldsymbol{R}(\boldsymbol{u}). \tag{1}$$

where $\boldsymbol{u} = \boldsymbol{u}(\boldsymbol{x}, t), \boldsymbol{x} \in \Omega$ denotes a vector of the coefficients associated with the orthonormal basis in space, and $\boldsymbol{R}(\boldsymbol{u})$ the corresponding right-hand side of the semi-discrete equations of a spatial discretization. Without loss of generality, let us focus on a single time step $t \in [t_n, t_{n+1}]$.

Splitting the right-hand term of (1), we have

$$\frac{d\boldsymbol{u}}{dt} = \boldsymbol{J}_n\boldsymbol{u} + \boldsymbol{N}(\boldsymbol{u}), \tag{2}$$

where $\boldsymbol{J}_n = \mathrm{D}_u\boldsymbol{R}(\boldsymbol{u}_n)$ denotes the Jacobian matrix of $\boldsymbol{R}$, $\boldsymbol{N}(\boldsymbol{u}) = \boldsymbol{R}(\boldsymbol{u}) - \boldsymbol{J}_n\boldsymbol{u}$ is the remainder and the subscript n denotes the variable evaluated at the current time t_n, which has an integral solution

$$\boldsymbol{u}_{n+1} = e^{\Delta t\boldsymbol{J}_n}\,\boldsymbol{u}_n + e^{\Delta t\boldsymbol{J}_n}\int_0^{\Delta t} e^{-\tau\boldsymbol{J}_n}\boldsymbol{N}(\boldsymbol{u}(\boldsymbol{x}, t_n+\tau))\,d\tau \tag{3}$$

The PCEXP scheme is base on the formula (3), where the stiff part is computed analytically and the nonlinear term is approximated by a numerical method. Here we do the Taylor expansion about τ to the nonlinear term

$$\boldsymbol{N}(\boldsymbol{u}(\boldsymbol{x}, t_n+\tau)) = \sum_{k=0}^{\infty}\frac{\tau^k}{k!}\frac{\partial^k\boldsymbol{N}(\boldsymbol{u}_n)}{\partial\tau^k}, \tag{4}$$

after substituting (4) into (3) , we have

$$\boldsymbol{u}_{n+1} = e^{\Delta t\boldsymbol{J}_n}\,\boldsymbol{u}_n + \sum_{k=0}^{\infty}\frac{\partial^k\boldsymbol{N}(\boldsymbol{u}_n)}{\partial\tau^k}\int_0^{\Delta t}\frac{\tau^k}{k!}\,e^{(\Delta t-\tau)\boldsymbol{J}_n}\,d\tau. \tag{5}$$

Introducing a new function defined by

$$\phi_k(\Delta t\boldsymbol{J}_n) = \frac{1}{\Delta t^k}\int_0^{\Delta t} e^{(\Delta t-\tau)\boldsymbol{J}_n}\frac{\tau^{k-1}}{(k-1)!}\,d\tau, \tag{6}$$

Equation (5) can be expressed as a composition of linear combinations of products of ϕ_k functions

$$\boldsymbol{u}_{n+1} = e^{\Delta t\boldsymbol{J}_n}\,\boldsymbol{u}_n + \sum_{k=1}^{\infty}\Delta t^k\,\phi_k(\Delta t\boldsymbol{J}_n)\frac{\partial^{k-1}\boldsymbol{N}(\boldsymbol{u}_n)}{\partial\tau^{k-1}}. \tag{7}$$

Taking $k = 1$ gives the constant approximation to $\boldsymbol{N}$ in $[t_n, t_{n+1}]$, namely

$$\boldsymbol{N}(\boldsymbol{u}(\boldsymbol{x}, t_n+\tau)) \approx \boldsymbol{N}(\boldsymbol{u}_n) = \boldsymbol{R}(\boldsymbol{u}_n) - \boldsymbol{J}_n\,\boldsymbol{u}_n \tag{8}$$

Substituting (8) into (7) results in the first-order exponential scheme

$$\begin{aligned}\boldsymbol{u}_{n+1} &= e^{\Delta t\boldsymbol{J}_n}\boldsymbol{u}_n + \Delta t\,\phi_1(\Delta t\boldsymbol{J}_n)\,\boldsymbol{N}(\boldsymbol{u}_n)\\ &= \boldsymbol{u}_n + \Delta t\,\phi_1(\Delta t\boldsymbol{J}_n)\,\boldsymbol{R}(\boldsymbol{u}_n).\end{aligned} \tag{9}$$

This is also named as the first-order exponential time differencing (ETD1) scheme.[6,7] The second-order scheme ETD2[6] can be obtained with $k = 2$. As a consequence, the ETD2 scheme requires the evaluation of ϕ_2 function, which is often hard to accurately compute. Instead, the second-order PCEXP scheme is introduced[1–3] for avoiding computing the ϕ_2 function, which is obviously expensive.

$$\boldsymbol{u}^* = \boldsymbol{u}_n + \Delta t\,\phi_1(\Delta t\boldsymbol{J}_n)\boldsymbol{R}(\boldsymbol{u}_n). \tag{10}$$

$$\boldsymbol{u}_{n+1} = \boldsymbol{u}^* + \frac{1}{2}\Delta t\,\phi_1(\Delta t\boldsymbol{J}_n)\left[(\boldsymbol{N}(\boldsymbol{u}^*) - \boldsymbol{N}(\boldsymbol{u}_n)\right]. \tag{11}$$

PCEXP is thus a two-stage method. In the first stage, the solution with the first-order formula (9) is used to predict a solution $\boldsymbol{u}^*$ of (10). Then, the $n+1$ time solution is computed by the predicted $\boldsymbol{u}^*$ plus an averaged nonlinear term with the frozen Jacobian $\boldsymbol{J}_n$, as expressed in (11). Notice that, PCEXP only require the t_n variables thus it is a one-step method which does not involve the computation of ϕ_2 function.

A. Implementation with the Krylov subspace method

The implementation of PCEXP scheme involves the evaluation of matrix-vector products, namely, the product of the exponential functions of the Jacobian and a vector, such as ϕ_1 times a vector $\boldsymbol{R}$ in (10). The directly computation of the ϕ function with the matrix inversion $\boldsymbol{J}^{-1}$ is prohibitively expensive to evaluate for large-scale problems.[1] Instead, we use the Krylov subspace method proposed in[8,9] to overcome the computational difficulties for large-scale CFD problems. The basic idea of the Krylov method is to project and approximate the multiplication of $e^{\Delta t \boldsymbol{J}}$ with any vector $\boldsymbol{N}$, which is typically very large, onto a small Krylov subspace, and then carry out the resulting exponential computation of much smaller matrices. To reveal the structure of ϕ function times a vector $\boldsymbol{N}$, by doing the Taylor series expansion to the exponential term

$$\boldsymbol{J}^{-1}\frac{e^{\Delta t\boldsymbol{J}}-\boldsymbol{I}}{\Delta t}\boldsymbol{N}=\left(\boldsymbol{I}+\frac{(\Delta t\boldsymbol{J})}{2!}+\frac{(\Delta t\boldsymbol{J})^2}{3!}+\frac{(\Delta t\boldsymbol{J})^3}{4!}+\cdots\right)\boldsymbol{N}, \tag{12}$$

one can see that it can be regarded as a function projection onto the Krylov subspace of dimension m,

$$K_m(\boldsymbol{J},\boldsymbol{N})=span\{\boldsymbol{N},\boldsymbol{J}\boldsymbol{N},\boldsymbol{J}^2\boldsymbol{N},\cdots,\boldsymbol{J}^{m-1}\boldsymbol{N}\}. \tag{13}$$

In the Krylov subspace method, orthogonal basis $\boldsymbol{V}_m=[\boldsymbol{v}_1,\boldsymbol{v}_2,\cdots,\boldsymbol{v}_m]$ of $\mathbb{K}_m$ can be obtained by the well known Arnoldi's algorithm outlined in Algorithm 1.

Algorithm 1 Arnoldi's process

```
Initialize v_1 = N/||N||_2
for j = 1 to m do
  w = J v_j
  for i = 1 to j do
    h_{i,j} = (w, v_i)
    w = w − h_{i,j} v_i
  end for
  h_{i+1,j} = ||w||_2
  v_{j+1} = w/h_{i+1,j}
end for
```

The computed $\boldsymbol{V}_m$ satisfies the so-called Arnoldi decomposition[9]

$$\boldsymbol{J}\boldsymbol{V}_m=\boldsymbol{V}_{m+1}\widetilde{\boldsymbol{H}}_m, \tag{14}$$

where $\boldsymbol{V}_{m+1}$ is of the dimension $m\times(m+1)$ and $\widetilde{\boldsymbol{H}}_m$ is a $(m+1)\times m$ upper-Heisenberg matrix of the form

If let $\boldsymbol{H}_m$ denotes the matrix composed of the first m rows of $\widetilde{\boldsymbol{H}}_m$ and $\mathrm{e_m}=[0,\cdots,0,1]^{\mathrm{T}}$ be the last canonical basis, we have

$$\boldsymbol{J}\boldsymbol{V}_m=\boldsymbol{V}_m\boldsymbol{H}_m+h_{m+1,m}\boldsymbol{v}_{m+1}\mathrm{e}_m^T \tag{15}$$

Because $\boldsymbol{V}_m^T\boldsymbol{V}_m=\boldsymbol{I}$, we have

$$\boldsymbol{H}_m=\boldsymbol{V}_m^T\boldsymbol{J}\boldsymbol{V}_m. \tag{16}$$

Therefore $\boldsymbol{H}_m$ represents the projection of the linear transformation of $\boldsymbol{J}$ onto the subspace K_m, with respect to the basis $\boldsymbol{V}_m$. Based on this, the following approximation was introduced

$$e^{\boldsymbol{J}}\boldsymbol{N}\approx e^{\boldsymbol{V}_m\boldsymbol{H}_m\boldsymbol{V}_m^T}\boldsymbol{N}=\boldsymbol{V}_m e^{\boldsymbol{H}_m}\boldsymbol{V}_m^T\boldsymbol{N}. \tag{17}$$

Since the first column vector of $\boldsymbol{V}_m$ is $\boldsymbol{v}_1=\boldsymbol{N}/||\boldsymbol{N}||_2$, we can use $\boldsymbol{V}_m^T=||\boldsymbol{N}||_2\,e_1$ with $e_1=[1,0,\cdots,1]$ to simply (17) as

$$e^{\boldsymbol{J}}\boldsymbol{N}\approx||\boldsymbol{N}||_2\boldsymbol{V}_m e^{\boldsymbol{H}_m}e_1. \tag{18}$$

Since $\boldsymbol{V}_m^T(\alpha\boldsymbol{J})=\alpha\boldsymbol{H}_m$, the Krylov subspaces associated with $\boldsymbol{J}$ and $\alpha\boldsymbol{J}$ are identical, thus

$$e^{\alpha\boldsymbol{J}}\boldsymbol{N}\approx||\boldsymbol{N}||_2\boldsymbol{V}_m e^{\alpha\boldsymbol{H}_m}e_1. \tag{19}$$

Thus the ϕ_1 function can be approximated as

$$\phi_1(\Delta t\boldsymbol{J})\boldsymbol{N}=\frac{1}{\Delta t}\int_0^{\Delta t}e^{(\Delta t-\tau)\boldsymbol{J}}\boldsymbol{N}\,d\tau\approx\frac{1}{\Delta t}\int_0^{\Delta t}||\boldsymbol{N}||_2\boldsymbol{V}_m e^{(\Delta t-\tau)\boldsymbol{H}_m}e_1\,d\tau. \tag{20}$$

Therefore, we obtain

$$\phi_1(\Delta t\boldsymbol{J})\boldsymbol{N} \approx \frac{1}{\Delta t}||\boldsymbol{N}||_2\boldsymbol{V}_m\int_0^{\Delta t} e^{(\Delta t-\tau)\boldsymbol{H}_m}e_1\,d\tau \tag{21}$$

$$= \frac{1}{\Delta t}||\boldsymbol{N}||_2\boldsymbol{V}_m\boldsymbol{H}_m^{-1}(e^{\Delta t\boldsymbol{H}_m}-\boldsymbol{I})e_1. \tag{22}$$

The dimension of Krylov subspace m is much smaller than the dimension of $\boldsymbol{J}$, so that $e^{\Delta t\boldsymbol{H}_m}$ in (22) can be computed very easily. In our tests the Chebyshev rational approximation with $p = 14$ is used for $e^{-\Delta t\boldsymbol{H}_m}$, as in references.[9]

B. Analytical viscous Jacobian matrices

The accuracy and stability of the PCEXP scheme rely on the the accuracy of approximating the Jacobian matrix $\boldsymbol{J}$, which is directly determined by the local truncation error analysis.[1] In the PCEXP scheme, the broadcasting of global information containing the exact roadmap of flow transportation is achieved through the introduction of exact Jacobian which accurately includes the convection and diffusion behavior of both the interior and boundary elements.

To compute the Jacobians exactly, we start with the right-hand term of (1) by using a discontinuous Galerkin spatial discretization[2] with one extra term, the lifting operator $\boldsymbol{\delta}$ due to the BR2 scheme[10]

$$\boldsymbol{R}_i = -\int_\Omega \psi_i\,\widetilde{\boldsymbol{F}}\,d\boldsymbol{\sigma} + \int_\Omega (\,\boldsymbol{\nabla}\psi_i\boldsymbol{F}(\boldsymbol{U}+\boldsymbol{\delta}) + \psi_i\,\boldsymbol{S}\,)\,d\boldsymbol{x} \tag{23}$$

The surface flux $\widetilde{\boldsymbol{F}}$ (24) consisting of convection and the diffusion terms is computed with the Roe's Riemann flux solver[11] and the BR2 viscous flux,[10] respectively

$$\widetilde{\boldsymbol{F}} = \widetilde{\boldsymbol{F}}_{\text{invis}}(\boldsymbol{U}_L,\boldsymbol{U}_R) + \widetilde{\boldsymbol{F}}_{\text{vis}}(\boldsymbol{U}_L,\boldsymbol{U}_R,\boldsymbol{\nabla}U_L+\boldsymbol{\delta}_L,\boldsymbol{\nabla}U_R+\boldsymbol{\delta}_R). \tag{24}$$

The residual Jacobian is so complicated that we have to broke it into several steps. First of all, let us consider the diagonal Jacobians. They are obtained by taking the derivative of (23) with respect to $\boldsymbol{u}_j$ of the host cell with the superscript or subscript L, and $\psi = \psi^L$

$$\begin{aligned}\frac{\partial\boldsymbol{R}_i}{\partial\boldsymbol{u}_j^L} &= -\int_{\partial\Omega}\psi_i\frac{\partial\widetilde{\boldsymbol{F}}}{\partial\boldsymbol{u}_j^L}\,d\boldsymbol{\sigma} + \int_\Omega\left(\boldsymbol{\nabla}\psi_i\frac{\partial\boldsymbol{F}(\boldsymbol{U}+\boldsymbol{\delta})}{\partial\boldsymbol{U}}\frac{\partial\boldsymbol{U}}{\partial\boldsymbol{u}_j^L} + \psi_i\frac{\partial\boldsymbol{S}}{\partial\boldsymbol{U}}\frac{\partial\boldsymbol{U}}{\partial\boldsymbol{u}_j^L}\right)d\boldsymbol{x}\\ &= -\int_{\partial\Omega}\psi_i^L\,\psi_j^L\frac{\partial\widetilde{\boldsymbol{F}}}{\partial\boldsymbol{u}_j^L}\,d\boldsymbol{\sigma} + \int_\Omega\left(\psi_j^L\,\boldsymbol{\nabla}\psi_i^L\frac{\partial\boldsymbol{F}(\boldsymbol{U}+\boldsymbol{\delta})}{\partial\boldsymbol{U}} + \psi_i^L\,\psi_j^L\frac{\partial\boldsymbol{S}}{\partial\boldsymbol{U}}\right)d\boldsymbol{x}.\end{aligned} \tag{25}$$

where it is found that $\partial\boldsymbol{\delta}/\partial\boldsymbol{U}$ in the volume integration does not show any effect on accuracy, stability enhancement and performance gain. As such, $\partial\boldsymbol{\delta}/\partial\boldsymbol{U}$ in the volume integration is omitted, contributing cost reduction for the overall performance of PCEXP. The rest volume Jacobians such as $\partial\boldsymbol{F}(\boldsymbol{U}+\boldsymbol{\delta})/\partial\boldsymbol{U}$ and $\partial\boldsymbol{S}/\partial\boldsymbol{U}$ are easy to evaluate analytically.

In (25), the surface Jacobian $\partial\widetilde{\boldsymbol{F}}/\partial\boldsymbol{u}_j^L$ is hard to be obtained immediately, so we apply the chain-differential law to (24)

$$\begin{aligned}\frac{\partial\widetilde{\boldsymbol{F}}}{\partial\boldsymbol{u}_j^L} &= \frac{\partial\widetilde{\boldsymbol{F}}_{\text{invis}}}{\partial\boldsymbol{U}_L}\frac{\partial\boldsymbol{U}_L}{\partial\boldsymbol{u}_j^L} + \frac{\partial\widetilde{\boldsymbol{F}}_{\text{vis}}}{\partial\boldsymbol{\nabla}U_L}\left(\frac{\partial\boldsymbol{\nabla}U_L}{\partial\boldsymbol{u}_j^L} + \frac{\partial\boldsymbol{\delta}_L}{\partial\boldsymbol{u}_j^L}\right) + \frac{\partial\widetilde{\boldsymbol{F}}_{\text{vis}}}{\partial\boldsymbol{\nabla}U_R}\frac{\partial\boldsymbol{\delta}_R}{\partial\boldsymbol{u}_j^L}\\ &= \frac{\partial\widetilde{\boldsymbol{F}}_{\text{invis}}}{\partial\boldsymbol{U}_L}\psi_j^L + \frac{\partial\widetilde{\boldsymbol{F}}_{\text{vis}}}{\partial\boldsymbol{\nabla}U_L}\left(\boldsymbol{\nabla}\psi_j^L\mathbf{I} + \frac{\partial\boldsymbol{\delta}_L}{\partial\boldsymbol{u}_j^L}\right) + \frac{\partial\widetilde{\boldsymbol{F}}_{\text{vis}}}{\partial\boldsymbol{\nabla}U_R}\frac{\partial\boldsymbol{\delta}_R}{\partial\boldsymbol{u}_j^L},\end{aligned} \tag{26}$$

where the Jacobians $\partial\boldsymbol{\delta}_L/\partial\boldsymbol{u}_j^L$ and $\partial\boldsymbol{\delta}_R/\partial\boldsymbol{u}_j^L$ are derived exactly and they contain the most of viscous-discretization stabilizing effects therefore must not be omitted. Remaining Jacobians are evaluated exactly by Automatic Differentiation (AD) tools.

Similarly, the off-diagonal terms about the neighboring cells with the super or subscript R around the host cell L are evaluated in the same way

$$\begin{aligned}\frac{\partial \boldsymbol{R}_i}{\partial \boldsymbol{u}_j^R} &= -\int_{\partial\Omega} \psi_i \frac{\partial \widetilde{\boldsymbol{F}}}{\partial \boldsymbol{u}_j^R}\, d\boldsymbol{\sigma} + \int_{\Omega} \left(\boldsymbol{\nabla}\psi_i \frac{\partial \boldsymbol{F}(\boldsymbol{U}+\boldsymbol{\delta})}{\partial \boldsymbol{U}} \frac{\partial \boldsymbol{U}}{\partial \boldsymbol{u}_j^R} + \psi_i \frac{\partial \boldsymbol{S}}{\partial \boldsymbol{U}} \frac{\partial \boldsymbol{U}}{\partial \boldsymbol{u}_j^R} \right) d\boldsymbol{x} \\ &= -\int_{\partial\Omega} \psi_i^L\, \psi_j^R \frac{\partial \widetilde{\boldsymbol{F}}}{\partial \boldsymbol{u}_j^R}\, d\boldsymbol{\sigma} + \int_{\Omega} \left(\psi_j^R\, \boldsymbol{\nabla}\psi_i^L \frac{\partial \boldsymbol{F}(\boldsymbol{U}+\boldsymbol{\delta})}{\partial \boldsymbol{U}} + \psi_i^L\, \psi_j^R \frac{\partial \boldsymbol{S}}{\partial \boldsymbol{U}} \right) d\boldsymbol{x},\end{aligned} \tag{27}$$

where

$$\begin{aligned}\frac{\partial \widetilde{\boldsymbol{F}}}{\partial \boldsymbol{u}_j^R} &= \frac{\partial \widetilde{\boldsymbol{F}}_{\text{invis}}}{\partial \boldsymbol{U}_R} \frac{\partial \boldsymbol{U}_R}{\partial \boldsymbol{u}_j^R} + \frac{\partial \widetilde{\boldsymbol{F}}_{\text{vis}}}{\partial \boldsymbol{\nabla} U_R} \left(\frac{\partial \boldsymbol{\nabla} U_R}{\partial \boldsymbol{u}_j^R} + \frac{\partial \boldsymbol{\delta}_L}{\partial \boldsymbol{u}_j^R} \right) + \frac{\partial \widetilde{\boldsymbol{F}}_{\text{vis}}}{\partial \boldsymbol{\nabla} U_R} \frac{\partial \boldsymbol{\delta}_R}{\partial \boldsymbol{u}_j^R} \\ &= \frac{\partial \widetilde{\boldsymbol{F}}_{\text{invis}}}{\partial \boldsymbol{U}_R} \psi_j^R + \frac{\partial \widetilde{\boldsymbol{F}}_{\text{vis}}}{\partial \boldsymbol{\nabla} U_R} \left(\boldsymbol{\nabla}\psi_j^R \mathbf{I} + \frac{\partial \boldsymbol{\delta}_L}{\partial \boldsymbol{u}_j^R} \right) + \frac{\partial \widetilde{\boldsymbol{F}}_{\text{vis}}}{\partial \boldsymbol{\nabla} U_R} \frac{\partial \boldsymbol{\delta}_R}{\partial \boldsymbol{u}_j^R}.\end{aligned} \tag{28}$$

When $\boldsymbol{\sigma}$ is an interior face, the flux $\widetilde{\boldsymbol{F}}(\boldsymbol{U}_L, \boldsymbol{U}_R)$ is calculated by Roe's Riemann solver.[11] The Riemann flux Jacobian matrices of (25) and (26) are evaluated exactly through AD. When $\boldsymbol{\sigma}$ is a boundary face, using a corresponding boundary condition, one has

$$\widetilde{\boldsymbol{F}} = \widetilde{\boldsymbol{F}}_{\text{bc}}(\boldsymbol{U}_L, \boldsymbol{U}_{\text{ghost}}), \tag{29}$$

where $\boldsymbol{U}_{\text{ghost}}$ is a function of $\boldsymbol{U}_L$ with the corresponding boundary condition. We remark that this type of consistent and exact evaluation of the boundary Jacobians is essential for maintaining excellent stability and convergence. In details, it is obtained in the following way

$$\frac{\partial \widetilde{\boldsymbol{F}}}{\partial \boldsymbol{U}} = \frac{\partial \widetilde{\boldsymbol{F}}_{\text{bc}}}{\partial \boldsymbol{U}_L} + \frac{\partial \widetilde{\boldsymbol{F}}_{\text{bc}}}{\partial \boldsymbol{U}_{\text{ghost}}} \frac{\partial \boldsymbol{U}_{\text{ghost}}}{\partial \boldsymbol{U}_L}. \tag{30}$$

As same as the interior faces, $\widetilde{\boldsymbol{F}}_{\text{bc}}$ uses the same Roe's Riemann flux, and the Jacobian matrices $\partial\widetilde{\boldsymbol{F}}/\partial\boldsymbol{U}_L$, $\partial\boldsymbol{U}_{\text{ghost}}/\partial\boldsymbol{U}_L$ are also evaluated exactly by AD. Hence the computations of all the Jacobians in the whole domain are totally consistent, contributing very strong robustness and good convergence behaviors with arbitrarily high-order DG for all the flow regimes.

III. Numerical results

In this section, several test cases are presented to demonstrate the capability of solving the unsteady compressible Navier-Stokes equations. Time-dependent solutions are obtained by conducting the so-called time marching via the PCEXP scheme, where the time-step size Δt_n is determined by

$$\Delta t_n = \frac{\text{CFL}\,(n)\; h_{3\text{D}}}{(2p+1)\,(\|\boldsymbol{v}\| + c)}, \quad h_{3\text{D}} := 2d\frac{\|E\|}{\|\partial E\|}, \tag{31}$$

where $\text{CFL}\,(n)$ is the Courant-Friedrichs-Lewy (CFL) number: a function of the number of time steps n for steady flows according to the formula (33). p denotes the polynomial order of DG in space, $\boldsymbol{v}$ the velocity vector at the cell center, c the speed of sound, d the spatial dimension, $\|E\|$ and $\|\partial E\|$ the volume and the surface area of the boundary of E, respectively; and $h_{3\text{D}}$ represents a characteristic size of a cell in 3D defined by the ratio of its volume and surface area. For quasi-2D problems, we extrude a 2-D mesh to a 3-D (quasi-2D) mesh by one layer of elements and use $h_{2\text{D}}$ instead of $h_{3\text{d}}$ to eliminate the effect of the z dimension on obtaining the truly 2-D time step. Given the cell size Δz in the z direction, $h_{2\text{D}}$ is determined by

$$\frac{2}{h_{2\text{D}}} = \frac{3}{h_{3\text{D}}} - \frac{1}{\Delta z}. \tag{32}$$

The following CFL formula is used for a robust code start-up for unsteady flows, and it is bounded by the cap value $\text{CFL}_{\max}$

$$\text{CFL}(n) = \min\left\{ \text{CFL}_{\max},\, \max\left[\|R_\rho(\boldsymbol{u}_n)\|_2^{-1},\, 1 + \frac{(n-1)}{(2p+1)} \right] \right\}, \tag{33}$$

where $\|R_\rho(\boldsymbol{u}_n)\|_2 := \frac{1}{|\Omega|}\left[\int_\Omega R_\rho(\boldsymbol{u}_n)^2 d\boldsymbol{x}\right]^{\frac{1}{2}}$, $R_\rho(\boldsymbol{u}_n)$ and $|\Omega|$ denote the residual of density and the volume of entire computational domain.

For the space discretization, a modal discontinuous Galerkin method for arbitrarily shape elements is used.[1,5] All the algorithms are implemented and tested in the HA3D parallel DG solver developed by the first author. In this paper, the PCEXP time-marching solutions up to fourth order (p=3) DG are computed for time-dependent laminar and turbulence flows.

A. Unsteady rotating concentric cylinder flow

An analytical time-dependent laminar N-S solution is firstly considered. The problem is an incompressible viscous fluid between two concentric cylinders of radius r_0 and r_1. When $t = t_0$ the fluid is at rest and the two cylinders are suddenly given angular velocity ω_0 and ω_1. The flow satisfies the unsteady Navier-Stokes equations in cylindrical coordinates

$$\frac{\partial u_\theta}{\partial t} = \frac{\partial^2 u_\theta}{\partial r^2} + \frac{\partial [u_\theta / r]}{\partial r} \tag{34}$$

where t is non-dimensionalized with $T = r_0^2/\nu$, and ν is the kinematic viscosity coefficient. u_θ and r denote the tangential velocity and radial coordinate. Its steady solution u_s is written as

$$u_s = r_0\,\omega_0 \frac{r_1/r - r/r_1}{r_1/r_0 - r_0/r_1} + r_1\,\omega_1 \frac{r/r_0 - r_0/r}{r_1/r_0 - r_0/r_1} \tag{35}$$

where $r_0 = 1$ is the inner radius, $r_1 = 2$ is the outer radius, respectively. ω_0 and ω_1 is the angular velocity of the inner wall and the outer one. The analytical time-dependent solution can be obtained by the speration-of-variables method of the form

$$u_\theta(r,t) = u_s(r) - \sum_{n=1}^{\infty} A_n f_n(r) \exp\left(-q_n^2 t\right) \tag{36}$$

For each value of n, it leads to solve the Bessel's equation

$$\frac{\partial f(r)}{\partial r^2} + \frac{\partial [f(r)/r]}{\partial r} - q_n^2 f(r) = 0 \tag{37}$$

and the solution is

$$f_n(r) = \alpha_n J_1(q_n r) + \beta_n Y_1(q_n r) \tag{38}$$

Applying the boundary conditions $f_n(r_0) = 0$ and $f_n(r_1) = 0$ lead to a series of values of q_n and the ratio α_n/β_n. One can determine the weights A_n by projecting the steady solution u_s on the function $f_n(r)$. The analytical solution (36) is finally obtained by using a finite-term series expansion with $n = 20$. The Reynolds number is based on the tangential velocity of the inner spinning cylinder, which is taken as 10 for keeping laminar state. ω_0 is chosen such that the tangential velocity satisfies Ma = 0.05. Constant viscosity is used to allow the comparison with the incompressible solution. We consider two cases: one is for testing the correctness of the converged steady solution, the other is for testing the dynamic evolution of the boundary layer profile.

1. Converged steady-state solution of the rotating concentric cylinder flow

The steady-state solution of the rotating concentric cylinder flow is computed for verifying the convergence order of accuracy. An isothermal boundary condition is set on the inner cylinder with angular velocity ω_0 corresponding to Ma = 0.05. The outer cylinder is stationary at $\omega_1 = 0$ with an adiabatic wall boundary condition. Three sets of meshes are generated using successive mesh refinements. The quasi-2D coarsest mesh that consists of $20 \times 2 \times 1$ cells is generated by uniformly distributing grid nodes in both directions. We compute the steady numerical solutions using the PCEXP scheme and the BR2 viscous term discretization. Quadratic curved elements are used along the boundary surfaces. The L_2 error measured in Table 1 is computed as $\sqrt{\int (u-u_\theta)^2 d\Omega \Big/ \int d\Omega}$ integrating in the entire computational domain Ω, from which the formal order of accuracy is observed. These results validate the implementation of the BR2 viscous discretization and the use of curved elements as well.

Table 1. Validation of the order of accuracy on the three sets successive refined meshes for the Taylor Couette flow case. The convergence rates of the L_2 error ($\log_{10}$) agrees well with the idea ones, respectively.

	$p=0$		$p=1$		$p=2$		$p=3$	
mesh size	L_2 error	order	L_2 error	order	L_2 error	order	L_2 error	order
20×2	-1.841096	N/A	-2.303743	N/A	-3.561000	N/A	-4.522970	N/A
40×4	-2.271501	1.43	-3.044176	2.46	-4.625891	3.54	-5.783858	4.19
80×8	-2.687538	1.38	-3.788182	2.47	-5.557918	3.10	-6.999223	4.04

2. *Unsteady solutions of the rotating concentric cylinder flow*

The time-accurate solutions of the rotating concentric cylinder flow are computed for verifying the capability of computing unsteady viscous flows with the PCEXP scheme. The analytical solution (36) is used and compared to the PCEXP's on a large-aspect-ratio boundary layer mesh – see Figure 1 (left), having $40\times 40\times 1=1600$ quadratic hexahedral elements and the first boundary layer height is compressed to 0.001. The geometric stiffness induced by such a boundary layer meshing results in a severer time step restriction for explicit methods.[1] In this case, large time steps with CFL $=10^3$ are used, and the computed time-slice results are in good agreement with the analytical solutions at different time locations as shown in Figure 1 (right). As shown in Table 2, the PCEXP scheme allows few time steps for time-dependent stiff problems while maintaining time-accurate solutions at low relative errors ($<3\%$) measured by the L_2 norm of the tangential velocity.

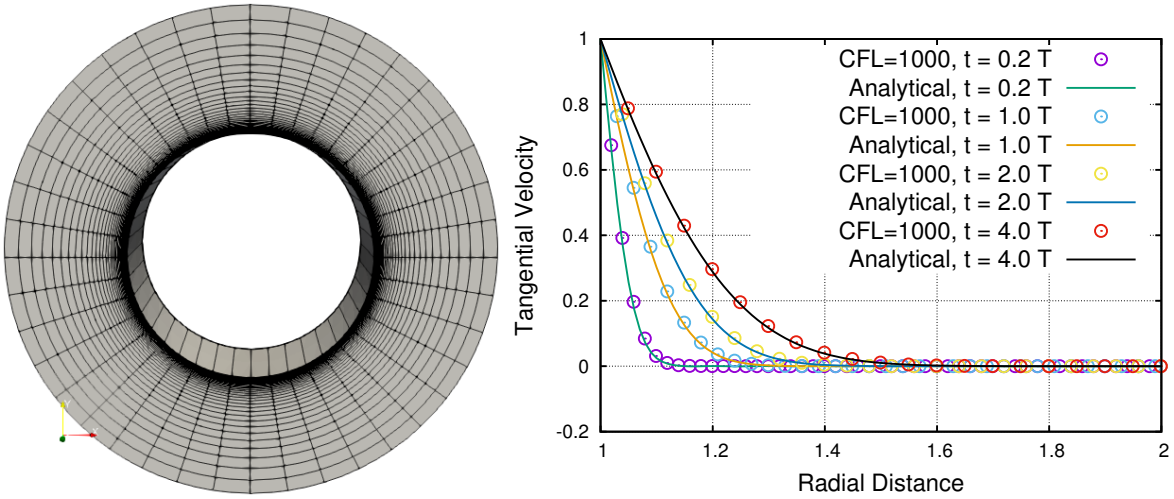

Figure 1. Quasi-2D large-aspect-ratio mesh and velocity profiles comparsion ($40\times 40\times 1=1600$ cells)

Table 2. Results statistics of the PCEXP scheme for the rotating concentric cylinder flow.

Time ($T=r_0^2/\nu$)	$0.2\,T$	$1.0\,T$	$2.0\,T$	$4.0\,T$
#Time steps	16	79	158	315
CFL	10^3	10^3	10^3	10^3
L_2 Error (%)	0.28	0.24	0.26	0.29

B. Unsteady laminar flows past a circular cylinder

The 2-D unsteady viscous flow benchmark problem: unsteady laminar flow past a circular cylinder is computed at Reynolds number $60, 80, 100, 120, 140, 160, 180$, based on the cylinder diameter. For $\mathrm{Re} \leq 180$, the flow is essentially two dimensional and alternating vortices are convected downstream from the cylinder, *i.e.*, the well known von Karman vortex street. The unsteady characteristic frequency expressed in dimensionless Strouhal number $\mathrm{St} = fd/U$ is computed by the PCEXP scheme and compared with the experimental results of Williamson and Brown[12] and the numerical results of Karniadakis[13] using a high-order spectral method, as shown in Table 3. Among which, the PCEXP results are computed with the fourth-order DG and PCEXP time marching on 3617 hybrid elements with the far-field boundary located 35 diameters away from the cylinder plus a buffer layer of 25 diameters wide filled by rectangle elements. The CFL number takes 500 for all the Reynolds numbers. Figure 3 gives the computed Karman vortex streets at $\mathrm{Re} = 60, 120, 180$. Different vortex patterns are showing which correspond to different Strouhal numbers. Table 3 shows the computed Strouhal number St and also the comparison to experimental[12] and numerical results,[13] again, they are fairly close to the references.

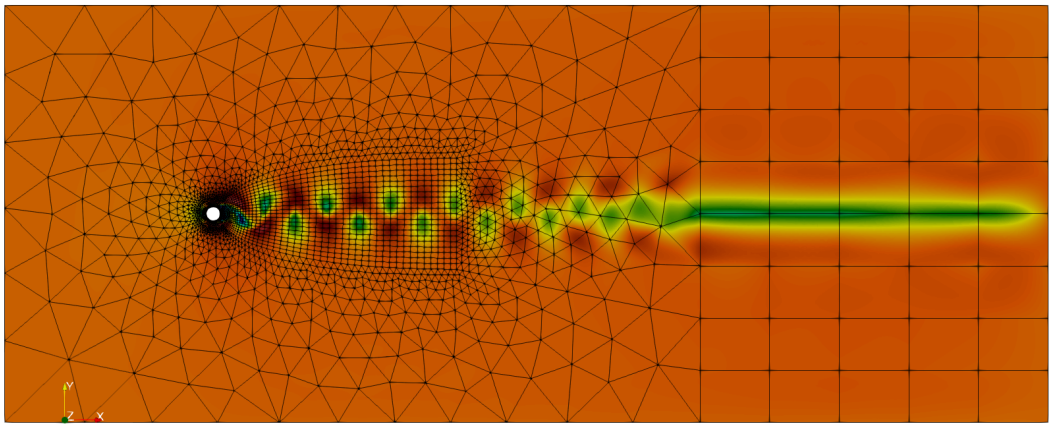

Figure 2. Hybrid grids and velocity contour for the laminar flow past a circular cylinder at Re = 180.

Table 3. Results statistics for the laminar flow past a circular cylinder.

Re	60	80	100	120	140	160	180
Present	0.139	0.155	0.168	0.178	0.185	0.191	0.197
Experiments[12]	0.135	0.152	0.164	0.173	0.181	0.186	N/A
Karniadakis[13]	0.153	0.168	0.178	0.185	0.192	0.197	0.203

C. Turbulent flow past a square cylinder at Ma = 0.15, Re = 22000

In this case, an implicit large eddy simulation (ILES) of turbulent flow past a 2-D square cylinder is computed by the PCEXP scheme as an illustrative example. Figure 4 shows the wake flow pattern captured with the DG $p = 4$ accuracy along with the PCEXP time-marching scheme. The instantaneous result shows a rather detailed turbulence structure, demonstrating the applicability of using PCEXP to turbulent flows which deserves a further research on it.

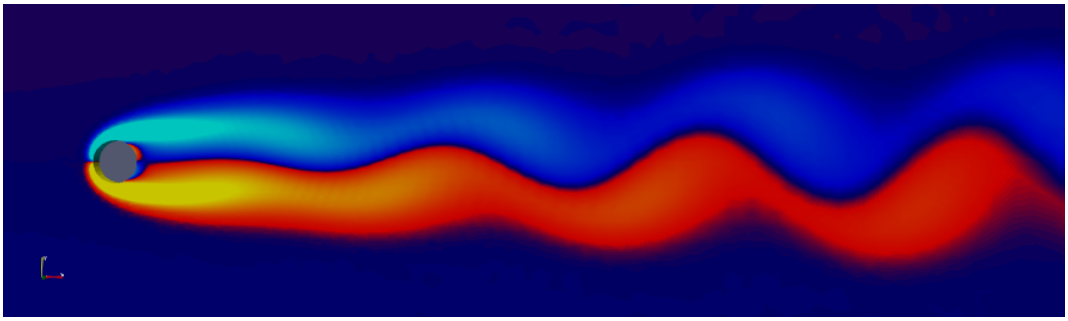

(a) Re = 60

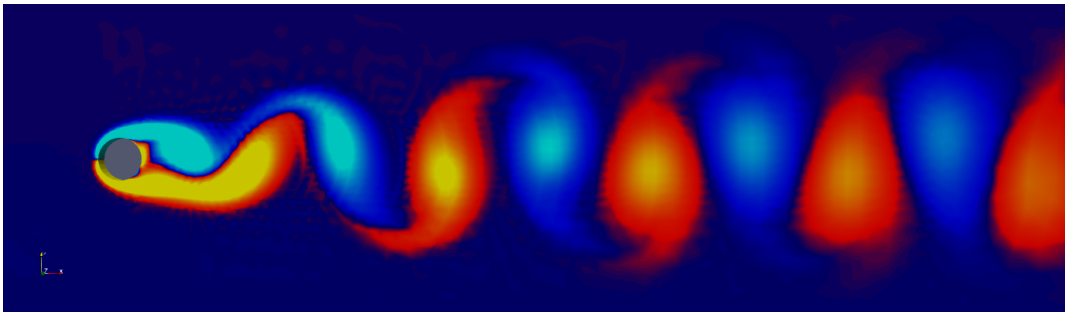

(b) Re = 120

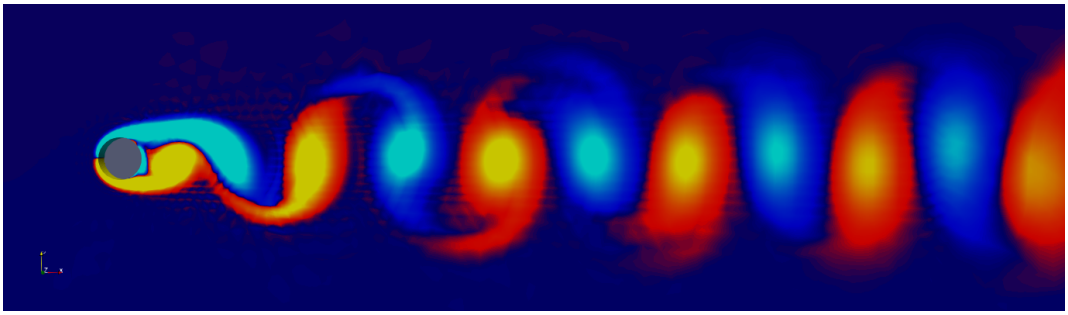

(c) Re = 180

Figure 3. Vorticity field for the laminar flow past a circular cylinder with CFL = 500.

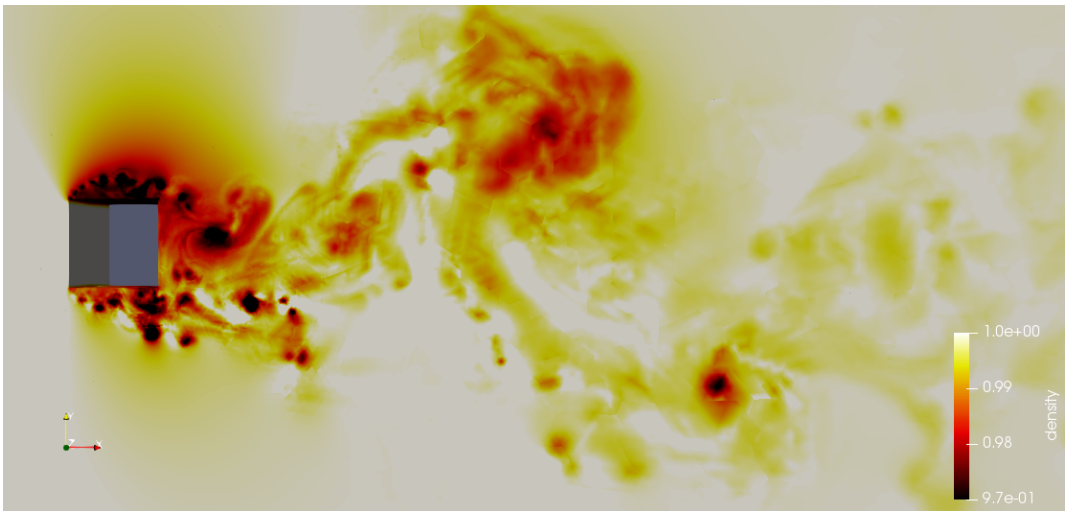

Figure 4. Turbulent flow field for the flow past a square cylinder: Ma = 0.15, Re = 22000, DG $p = 4$.

D. Flow past a sphere at Ma = 0.3, Re = 300

The 3-D unsteady laminar flow past a sphere at Ma = 0.3 is considered for demonstrating the applicability of PCEXP to 3-D unsteady flows. The Reynolds number Re = 300 is based on the sphere diameter $d = 2$ and far-field boundaries are located 50 diameters away from the sphere. The third-order DG is used for spatial discretization while the time marching is achieved by the PCEXP scheme using CFL = 500. The height of the first boundary layer is 0.05 and uniform edge size around 0.8 is used in the wake region. Very large cells sizing up to 20 are generated as a far-field buffer zone for damping the outflow structure as shown in Figure 5(a). The wake flow pattern is shown in Figure 5(a) and 5(b), where similar shed vortex structures are observed compared with the experimental photograph of Figure 6. The statistic results are given in Table 4 comparing with the reference results, where the present result is close to Gassner's $4th$-order spatial-temporal, high-resolution result.[14] Again, it shows the low temporal error feature of PCEXP as found in the previous study.[1]

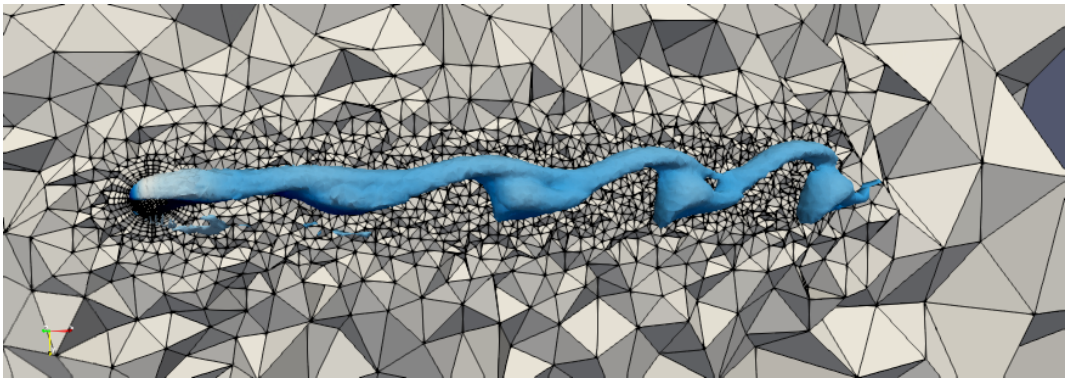

(a) Q contour colored by the velocity magnitude

(b) Velocity magnitude contour on the cut slice at $z = 0$

Figure 5. Computed wake structure for the flow past a sphere at Ma = 0.3, Re = 300.

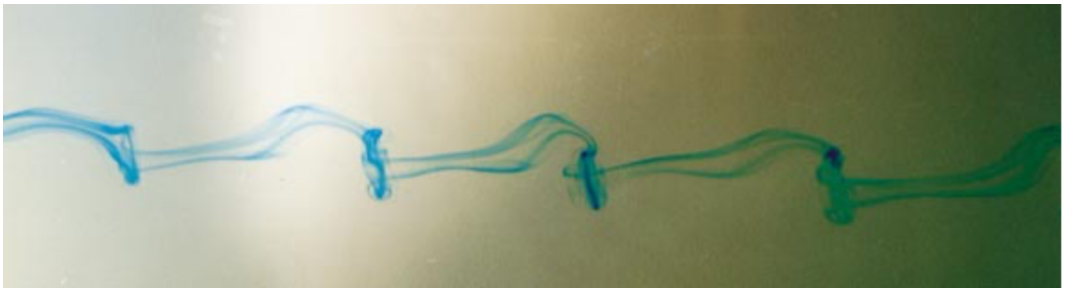

Figure 6. Experimental result[15] for the shed vortex structure of the flow past a sphere at Re = 300.

Method	#Cell	S_{order}	T_{order}	C_d	ΔC_d	St
Present	80093	$3rd$	$2nd$	0.674	0.0033	0.133
Gassner[14]	160000	$4th$	$4th$	0.673	0.0031	0.131
Johnson[15]	428442	$2nd$	$2nd$	0.656	0.0035	0.137
Haga[16]	54312	$4th$	$3rd$	0.670	0.0032	0.131

Table 4. Results statistics of the PCEXP scheme for the flow past a sphere at Re = 300.

IV. Conclusion

In this work, the Predictor-Corrector EXPonential time-integrator scheme (PCEXP)[1–3] is successfully applied to simulate time-dependent compressible viscous flows with high-order DG discretizations in space. Computational advantages of the PCEXP scheme for inviscid flows,[1,2] steady viscous flows[3] are consistently verified. Large time steps with CFL number from 5×10^2 to 1×10^3 are actually allowed for the test cases, significantly relieving the geometric stiffness induced by the high-aspect-ratio boundary layer elements. Numerical results exhibit that the PCEXP scheme can deliver time-accurate viscous flow solutions with correct unsteady characteristic frequencies for two- and three-dimensional CFD problems, offering an alternative method for the time discretization of high-order methods.

Acknowledgments

This work is support by the National Natural Science Foundation of China (NSFC) under the Grant number U1530401. LLJ acknowledge the support from the US National Science Foundation under the Grant DMS-1818438 and the US Department of Energy under the Grant DE-SC0016540. SJL would like to thank Prof. Pierre Lallemand for his valuable comments on the test cases.

References

[1]Li, S.-J., Luo, L.-S., Wang, Z.J., and Ju, L,"An exponential time-integrator scheme for steady and unsteady inviscid flows", J. Comput. Phys., 365 (2018): 206–225.

[2]Li, S.-J., Wang, Z.J., Ju, L., and Luo, L.-S., "Explicit Large Time Stepping with A Second-Order Exponential Time Integrator Scheme for Unsteady and Steady Flows", AIAA paper 2017–0753.

[3]Li, S.-J., Wang, Z.J., Ju, L., and Luo, L.-S., "Fast time integration of Navier-Stokes equations with an exponential-integrator scheme", AIAA paper 2018–0369.

[4]Li, S.-J, "Efficient p-multigrid method based on an exponential time discretization for compressible steady flows", arXiv:1807.0115.

[5]Li, S.-J, "A Parallel Discontinuous Galerkin Method with Physical Orthogonal Basis on Curved Elements", Procedia Engineering, 61(2013), 144–151.

[6]Cox, S.M., Matthews, P.C., "Exponential time differencing for stiff systems", J. Comput. Phys., 176 (2002): 430–455.

[7]Ju, L., Zhu, L.Y., Zhang, J., Du, Q., "Fast explicit integration factor methods for semilinear parabolic equations", J. Sci. Comput., 62 (2015): 431–455.

[8]Tokman, M., Loffeld, J., "Efficient design of exponential-Krylov integrators for large scale computing", Procedia Comput. Sci., 1 (2010): 229–237.

[9]Saad, Y., "Analysis of some Krylov subspace approximations to the matrix exponential operator", SIAM J. Numer., Anal., 29 (1992): 209–228.

[10]Bassi. F., Rebay. S., "A high-order accurate discontinuous finite element method for the numerical solution of the compressible Navier-Stokes equations",. J. Comput. Phys., 131(2) (1997) 267–279.

[11]Roe. P.L.,"Approximate Riemann solvers, parameter vectors, and difference schemes",J. Comput. Phys., 43(2) (1981) 357–372.

[12]Williamson, C. H. K., "Oblique and parallel modes of vortex shedding in the wake of a circular cylinder at low Reynolds number". J. Fluid Mech. 206(1989): 579–627.

[13]Karniadakis, G.E., Triantafyllou, G.S., "Frequency selection and asymptotic states in laminar wakes". J . Fluid Mech. 199(1989): 441–469.

[14]Gassner, G. J., Lorcher, F., Munz, C-D., et al., "Polymorphic nodal elements and their application in discontinuous Galerkin methods", J. Comput. Phys., 228 (2009): 1573–1590.

[15]Johnson, T. A., Patel, V. C., "Flow past a sphere up to a Reynolds number of 300", J. Fluid Mech., 378 (1999), 19-70.

[16]Haga, T., Gao, H., Wang, Z.J., "A High-Order Unifying Discontinuous Formulation for the Navier-Stokes Equations on 3D Mixed Grids", Math. Model. Nat. Phenom. 6 (2011): 28–56.